Structure and properties of the (100) surface of the Au-Si-Ho quasicrystalline approximant

Wilfried Bajoun Mbajoun ◉

Institut Jean Lamour, Université de Lorraine, UMR7198-CNRS, Campus ARTEM, Nancy, France

Yu-Chin Huang ◉

Department of Chemistry-Ångström Laboratory, Uppsala University, SE-751 21 Uppsala, Sweden

Girma Hailu Gebresenbut and Cesar Pay Gómez ◉

Department of Chemistry-Ångström Laboratory, Uppsala University, SE-751 21 Uppsala, Sweden

Emilie Gaudry ◉, Sylvie Migot-Choux ◉, Jaafar Ghanbaja ◉, Vincent Fournée ◉, and Julian Ledieu ◉

Institut Jean Lamour, Université de Lorraine, UMR7198-CNRS, Campus ARTEM, Nancy, France

The atomic structure and electronic properties of the (100) surface of the Au-Si-Ho Tsai-type quasicrystalline approximant has been investigated under ultrahigh vacuum conditions. After annealing the sample between 853 K and 878 K, Au-Si-Ho(100) exhibits a (2×1) surface reconstruction with a topography described by large terraces separated by a single step height equal to half the unit-cell parameter. The surface appears to terminate at specific bulk planes intercepting the Tsai-type clusters at their center. The electronic density of states is dominated by the $5d$ states of Au below the Fermi level and by the $5d$ states of Ho above the Fermi level with a metalliclike Fermi edge.

I. INTRODUCTION

Quasicrystals (QCs) are long-range ordered systems that lack the translational periodicity of usual crystals [1]. With no unit cell in three-dimensional space, their structure is often best described in physical space by the assembly of highly symmetric atomic clusters. The same concept of cluster assembly also applies to the atomic arrangement for the so-called quasicrystalline approximants, that are periodic crystals characterized by a large unit cell and a local atomic order that is similar to that of the parent quasicrystalline phase.

A precise knowledge of the surface crystalline structure is a prerequisite for understanding the surface properties of quasicrystals such as their low friction, low adhesion, corrosion resistance, and catalytic activity [2–5]. Most previous surface studies of aperiodic compounds have focused on stable Al-based QCs whose atomic structure is described in terms of pseudo-Mackay and Bergman clusters [6,7]. A general trend concluded from these studies is that surface phenomena present on crystals such as facet formation, terrace formation, bulk truncated termination, and surface relaxation also appear in quasicrystals [8–12].

The chemical disorder present in icosahedral (i)-QCs, which are mostly ternary alloys, is a hindrance to a complete description of their bulk structures. The discovery of the first stable binary i-QC in the Cd-Yb system together with different quasicrystalline approximants was an important step in determining their detailed atomic structure [13]. The cluster building blocks of this new class of QCs and their related periodic approximants consist in concentric polyhedral shells,

with an inner disordered tetrahedron at its center, followed by a dodecahedron, an icosahedron, an icosidodecahedron, and a rhombic triacontahedron [14]. These clusters are termed Tsai-type clusters in the literature. Due to the high vapor pressure of cadmium, the surface study of the Cd-Yb QC is incompatible with an ultrahigh vacuum (UHV) environment. However, it has been shown that isoelectronic substitutions lead to many different QC or approximant compounds with composition $(D_{(1-x)}P_x)_y$ RE, y ranging from 6 to 9, with D = Zn, Cd, Cu, Ag, Au, or Pd, P = Mg, Al, Ga, In, Sn, Ge, or Si, and RE = rare earth, Ca, or Sr [15]. Thus, by replacing Cd with Ag and In, the resulting i-Ag-In-Yb QC is isostructural to Cd-Yb and is suitable for UHV studies.

The structural study of the three high-symmetry surfaces of Ag-In-Yb shows that after sputtering and annealing under UHV, the surface consists of large terraces separated by specific atomic steps [16–18], corresponding to precise bulk truncation. The surface is found to terminate at specific bulk planes that intersect the Tsai-type cluster centers for all three high-symmetry surfaces of Ag-In-Yb [16–18].

The Au-Si-RE (RE=Ho, Tb, Gd) approximants have a structure close to the $MCd_{5.7}$ (M=Ca, Yb) quasicrystal built from Tsai-type clusters [19]. A detailed structural study of these systems has shown that the central tetrahedron of the Tsai-type cluster can be replaced by a single RE atom upon small variations of the stoichiometry. This new cluster is called a pseudo-Tsai cluster [20]. Due to their complex structure, Au-Si-RE approximants have unique thermoelectric and magnetic properties which can be modulated according to the chemical decoration of the cluster centers. It is

possible to have both Tsai clusters and pseudo-Tsai clusters randomly distributed in Au-Si-RE compounds. The presence of pseudo-Tsai clusters in the structure is accompanied by a decrease in both the lattice parameter and the magnetic transition temperature. The magnetic structure of the compound is modified according to the rate occupancy of the pseudo-Tsai cluster, inducing magnetic frustration and disorder in the system [19–22].

Unlike the bulk, the surface atomic structure and properties of Au-Si-RE systems remain unexplored with the exception of a recent study revealing Ho and Si co-segregation at the Au-Si-Ho(100) surface upon O_2 adsorption [23]. Several key questions are awaiting answers including the influence of the cluster-center decoration on the surface-plane selection and on the structural stability of surface layers. To this end, we report the characterization of the (100) surface of the Au-Si-Ho Tsai-type 1/1 approximant using both experimental techniques and density-functional theory (DFT)-based methods.

II. EXPERIMENTAL DETAILS

The single crystal Au-Si-Ho used in this study has been synthesized using a self-flux technique [19]. Powder x-ray diffraction (PXRD) was performed to determine the bulk structure, the latter being published in Ref. [19]. The crystal was oriented by back-reflection Laue x-ray diffraction. The cutout (100) surface has been mechanically polished to a mirrorlike finish using diamond paste with decreasing grain size down to 1/4 µm. After mounting the sample on a tantalum plate, it is investigated under a multichamber UHV system where the base pressure was 6×10^{-11} mbar. The surface preparation has consisted of Ar^+ ion sputtering at 2 kV for 30 min followed by 90 min annealing between 761 K and 878 K. The temperature was measured using an optical pyrometer with an emissivity set to 0.1 which is close to that of Au. The cleanliness, the evolution of the chemical composition with the annealing temperature, as well as a function of the photoelectron take-off angle measured with respect to the surface normal were monitored by x-ray photoelectron spectroscopy (XPS). The XPS spectra have been measured using a nonmonochromatized Mg K_α x-ray source (1253.6 eV). The electronic structure of the surface was measured by ultraviolet photoelectron spectroscopy (UPS) using a monochromatized He II photon source (40.8 eV). Low-energy electron diffraction (LEED) was used to monitor the quality of the long-range surface order and the surface-crystal symmetry. The morphology and the local atomic arrangement at the surface have been investigated by scanning-tunneling microscopy (STM) at room temperature. An electron-transparent lamella has been extracted from the sample by focus ion beam-scanning electron microscope (FIB-SEM, Helios NanoLab 600i, FEI, Eindhoven, The Netherlands) using Ga ions. The specimen was characterized by transmission electron microscopy (TEM) using a Cs-aberration-corrected probe (JEM-ARM 200CF; JEOL, Tokyo, Japan) operated at 200 keV, with a spatial resolution in STEM mode of 0.08 nm. The structure of the bulk has been investigated by high-angle annular dark-field scanning transmission electron microscopy (HAADF-STEM) images, selected-area electron diffraction (SAED), and compared with the results obtained from PXRD.

III. COMPUTATIONAL DETAILS

Electronic structure calculations were performed with the plane-wave Vienna *ab initio* simulation package (VASP) [24–27], using the projector augmented-wave (PAW) method [28,29] and the generalized gradient approximation (GGA-PBE) [30,31]. Eleven valence electrons were explicitly treated for Au ($5d^{10}6s^1$), 8 for Ho ($6s^25p^65d^0$) and 4 for Si ($3s^23p^2$). Total energies were minimized until the energy differences became less than 10^{-4} eV between two electronic cycles.

The bulk structure of the compound was built starting from the experimental structure, i.e., a cubic structure (space group 204). The lattice parameter is equal to 14.56 Å, and the compound is isostructural to the prototype Tsai-type 1/1 approximant crystal Cd_6Yb. The chemical disorder related to the presence of partial occupancy and two types of clusters (Tsai and pseudo-Tsai) present in the bulk structure [Fig. 1(a)] are problematic for the first-principle calculations requiring periodic boundary conditions. Thus, due to calculation requirements, all cluster centers have been filled with a Ho atom (no tetrahedron has been implemented at the cluster centers), departing from the experimentally determined structure. We used the supercell code [32] to generate typical structures accounting for the partial occupancies. One of these has been picked up randomly and further used for the electronic structure calculations based on the nonrelaxed system.

The structural model of the (100) surface has been implemented with 14.56 Å thick slabs separated by a 14.56 Å void thickness. We selected the flat plane, located at $z = 0$, as the termination plane. The STM images have been calculated using the slab built by numerical cleavage (without any structural optimization). We also optimized the structure with a criteria for the convergence based on atomic forces below 0.35 eV/Å.

IV. RESULTS AND DISCUSSION

A. Bulk structure

Figure 1(a) shows the bulk structure of Au-Si-Ho derived from PXRD analysis, projected along the [100] axis [19]. The atom positions are obtained from the cif file determined from PXRD. The Au-Si-Ho sample is a Tsai-type quasicrystalline approximant with a unit cell containing 173 atoms, including 116 Au atoms, 32 Si atoms, and 25 Ho atoms. Its chemical formula is $Au_{67.2}Si_{18.4}Ho_{14.4}$ (at.%). It crystallizes in a body-centered cubic structure (bcc) with a lattice parameter of 14.56 Å, and its space group is $Im\bar{3}$. At the cluster center surrounded by red circles in Fig. 1(a), there are both disordered tetrahedrons (made up of Au and Si) and Ho. The partial occupancies reflect that there is either a Ho or a disordered tetrahedron at these positions. In total, 48% of the clusters are of Tsai-type and 52% are of pseudo-Tsai type, and they are randomly distributed in the structure [21]. The densest (100) planes are those intercepting the cluster centers. The distance between two such consecutive planes along the [100] direction is half a unit cell, i.e., 7.28 Å.

To confirm the bulk structure given by PXRD, HAADF-STEM and SAED were performed. Figure 1(c) shows a SAED pattern obtained from the FIB lamella with complete symmetry (2 mm). The lattice parameter obtained from this
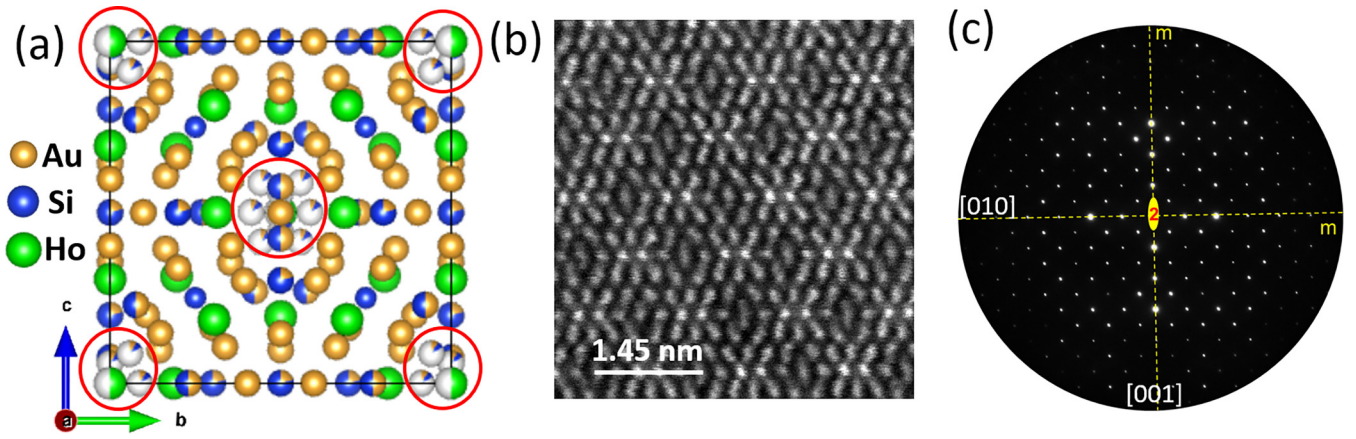
FIG. 1. (a) Bulk structure of Au-Si-Ho given by PXRD along the [100] axis. The yellow, blue, and green spheres represent Au, Si, and Ho atoms, respectively. White refers to vacancy. Multicolor spheres indicate partial occupancy rates of atomic sites. HAADF-STEM image (b) and SAED pattern (c) of the Au-Si-Ho lamellae recorded along the [001] zone axis, showing twofold axis and two-mirror planes across [010] and [001] directions.

diffraction pattern is 14.55 Å. In Fig. 1(b), the HAADF-STEM image has been recorded in the [100]-zone axis. It reveals atomic columns over the whole FIB lamella thickness. As expected from PXRD and the SAED pattern presented in Fig. 1(c), there is no superstructure observed at the nanoscale and no particular ordering related to the chemical decoration of the clusters. This has been further confirmed in a recent HAADF-STEM study on the same crystal [33].

B. Surface structure

1. Chemical analysis

We now concentrate on the structural and chemical characterization of the Au-Si-Ho(100) surface. The near-surface composition of the Au-Si-Ho(100) was estimated from XPS analysis of the core levels of Au $4f$, Si $2s$, Ho $4d$, after several sputtering and annealing cycles at a temperature of 878 K. Survey scan indicates that the surface is free from C and O contamination. Figure 2 shows the Ho $4d$ and Si $2s$ core-level XPS spectra of Au-Si-Ho(100). The close vicinity in binding energies of these two elements impacts the Ho $4d$ background,
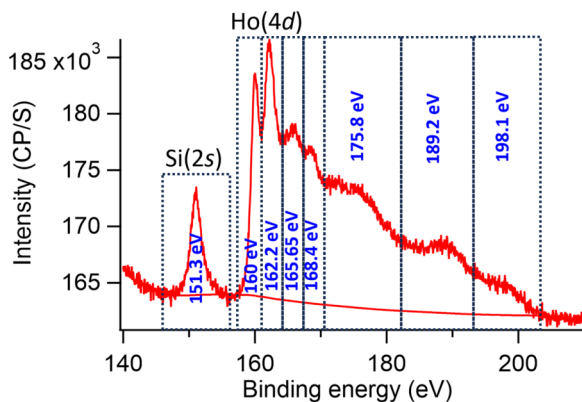
leading to difficulties in extracting the integrated intensity under the peak or leading to difficult peak fitting. The XPS spectrum of the Ho $4d$ extends over a region rich in features ranging from 157 eV to 210 eV. This spectrum consists of 7 peaks. Two sharp peaks appear at 160 and 162.2 eV, two other peaks with a lower intensity are observed at 165.65 and 168.4 eV, and three other broad peaks are present at 175.8, 189.2, and 198.1 eV. This Ho $4d$ spectrum in the Au-Si-Ho(100) sample is similar to the spectrum reported for HoB_4, $HoRh_3B$, and HoNi compounds [34–36], except that the broad peak at 198.10 eV is not as pronounced. In the HoB_4, the two peaks at 165.65 eV and 168.42 eV are attributed to satellite peaks coming from a different level of screening of the core hole created during the photoemission process. In HoNi, an atomic multiplet calculation was performed for Ho^{3+} and compared to the experimental spectrum. This calculation is in agreement with the Ho spectrum in Au-Si-Ho(100) and allows us to characterize this spectrum. It indicates that these peaks correspond to the atomic multiplets of Ho $4d$ and that inside the broad peak at 175.8 eV, there are plasmons.

The surface chemical composition has been estimated after annealing the sample at different temperatures. Angle-resolved XPS (AR-XPS) spectra were also recorded in order to vary the surface sensitivity of the measurements. The chemical composition of the surface is obtained from the Ho $4d$, Si $2s$, and Au $4f$ core-level spectra. To determine the area under each peak, a Shirley background was subtracted and satellite peaks induced by the MgK_α source were removed. The elemental concentrations are determined using the relationship

$$P_{X_0} = \frac{\frac{A_{X_0}}{N_{X_0}}}{\sum_{i=0}^{n} \frac{A_i}{N_{X_i}}} \times 100$$

where P_{X_0} is the atomic percentage of X_0, A_{X_0} is the area of X_0 peak, and N_{X_0} is the normalization factor associated to X_0. The normalization factor N_{X_i} contains all the corrections due to the element under study and due to the experimental set-up. $N_{X_i} = \lambda_{X_i} \times \sigma_{X_i} \times ATF_{X_i}$ with λ_{X_i} the electron mean-free path of X_i, σ_{X_i} the cross-section of X_i, and ATF_{X_i} the correction

FIG. 2. XPS measurements of the Ho $4d$ and Si $2s$ core-levels region. The highest peaks for Si and Ho multiplets have been highlighted in blue.
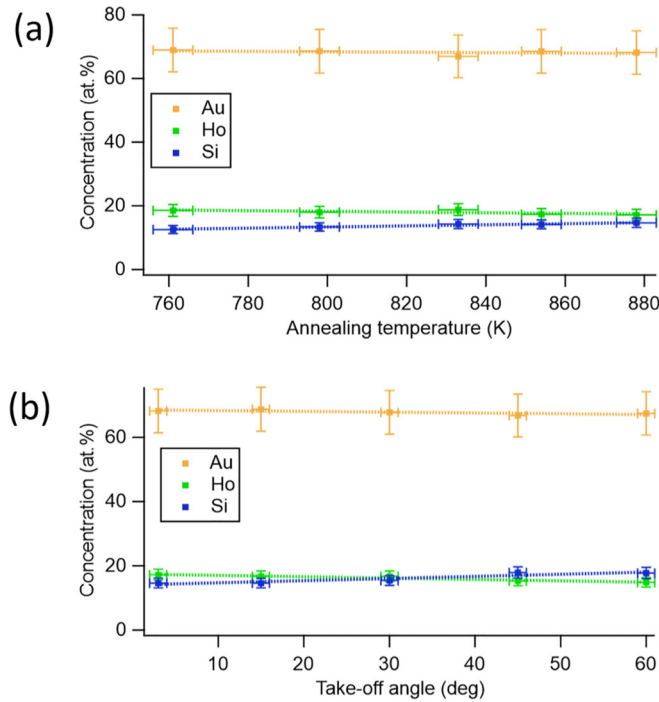
FIG. 3. (a) Variation of the elemental composition at the Au-Si-Ho(100) surface as a function of the annealing temperature. (b) Variation of the elemental composition as a function of the photoelectrons take-off angle for the sample annealed to 878 K. The dotted lines are linear fit to the data and are only guides for the eyes. The errors are estimated at $\pm$ 10% on the composition.
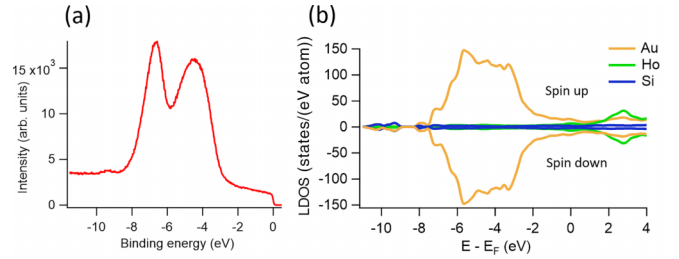

FIG. 4. (a) UPS valence-band structure of the Au-Si-Ho surface recorded using the He II UV source. (b) Partial electronic DOS calculated for the Au-Si-Ho bulk compound. As carried out, the calculation does not reveal any magnetization of the compound.

of the analyzer's transmission function. Figure 3(a) shows that the near-surface concentration is nearly constant in the annealing temperature range from 760 to 880 K, and close to the bulk value ($Au_{67.2}Si_{18.4}Ho_{14.4}$). The slight decrease in the Ho content (from 18.5 to 17.2 at.%) and the corresponding increase in Si (from 12.5 to 14.6 at.%) are below the estimated error bars ($\pm$ 10 at.%). The AR-XPS measurements after annealing the sample at 878 K [Fig. 3(b)] show a 3 at.% Si increase and a corresponding Ho decrease as the surface sensitivity is increased while the Au content remains constant. These variations are very small and we conclude that there is no surface segregation taking place in this system. The AR-XPS measurements also show that the core-level line shape of Au 4f, Si 2s, and Ho 4d are identical as the electron emission angle changes up to 60° indicating similar surface and bulk electronic structures for the electronic states associated with Au, Si, and Ho.

2. Electronic structure

The valence-band electronic structure of the clean surface has been investigated using UPS and *ab initio* methods. Figure 4(a) indicates that valence band structure is dominated by two main peaks at 4.2 and 7 eV below the Fermi level. This is in agreement with the partial electronic density of states (DOS) calculated for the Au-Si-Ho bulk compound [Fig. 4(b)]. The calculations reveal that the valence band is dominated by Au 5d states below the Fermi level and by Ho 5d states above the Fermi level. The experimental bands are

shifted by about 1 eV to lower binding energies compared to the calculated ones. These differences could be due to final-state effects in the photoemission process, to a surface effect, and/or correlations in Ho that are not taken into account in the calculations of the bulk DOS. The discrepancy between the calculated [Fig. 4(b)] and the experimental [Fig. 4(a)] valence band structures at -5.8 eV (dip) could be assigned to the surface reconstruction (He II is highly surface sensitive), whereas the calculations are performed for the bulk structure. We can conclude that contrary to the case of Ag-In-Yb where there is a pseudogap near the Fermi level [37], no reduction in the DOS is identified for the Au-Si-Ho system knowing that the calculation has been performed within the GGA-PBE approximation.

3. LEED pattern measurements

The crystallographic structure of the surface has been probed by LEED. After annealing the sample in the range between 853 and 878 K, the diffraction patterns exhibit sharp spots and a low background intensity as shown in Fig. 5(a), indicating a long-range ordered surface structure. The LEED pattern has been calibrated using diffraction patterns of a known crystalline structure recorded under identical experimental conditions. After calibration, the lattice parameters obtained are $b_s = 29.1 \pm 0.3$ Å and $c_s = 14.4 \pm 0.3$ Å. The lattice parameter obtained along the b axis is twice that expected from the bulk. Therefore the surface exhibits a (2 × 1) reconstruction that is not expected from bulk symmetry. LEED patterns do not reveal the formation of facets indicating the stability of the plan selected at the surface.

4. High-resolution STM images

After annealing the Au-Si-Ho(100) at 853 K, the surface has a step-terrace morphology with a single step height (7.4 $\pm$ 0.2 Å) approximately equal to half of the unit-cell parameter [Fig. 5(b)]; there is a selectivity of specific bulk planes as surface terminations. The calculated fast Fourier transform (FFT) of the STM image shown in Fig. 5(c) confirms the (2 × 1) reconstruction observed in the LEED pattern. The same image exhibits a shift of motifs or lines across consecutive terraces. In Fig. 5(d), a model of consecutive terraces separated by a 7.28 Å step height has been built from the bulk structure determined from PXRD analysis. As expected for a bcc structure, a shift in the motifs is observed across consecutive terraces separated by a height equal to $a/2$.
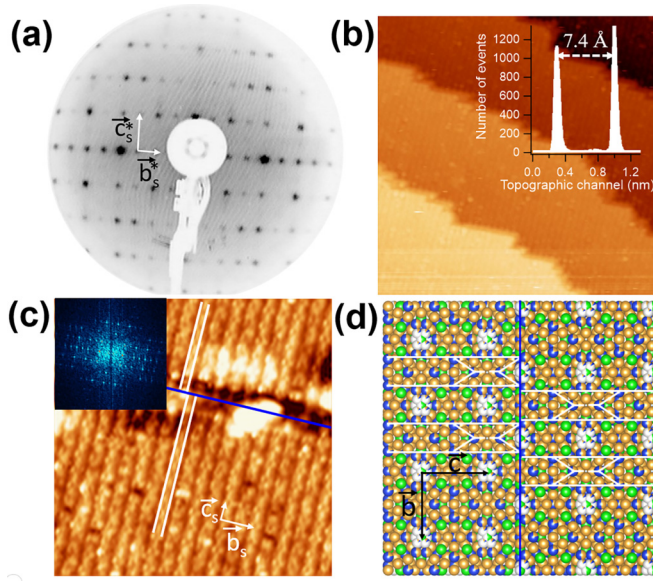
FIG. 5. (a) LEED pattern recorded at 22 eV after annealing the sample at 858 K. (b) STM image (100x100 nm^2, $V_b = -1.55$ V, $I_t = 0.13$ nA) presenting three successive terraces separated by a single-step height equal to 7.4 Å. (c) High-resolution STM image (100x100 nm^2, $V_b = -1.20$ V, $I_t = 0.26$ nA) showing a shift of motifs across consecutive terraces [Inset: FFT]. (d) Model of two consecutive surface terminations separated by steps of height equal to 7.28 Å (blue lines). Across each step, the structural motifs (head to tail Y motifs in white color) are shifted by half a unit cell along the [010] direction (as emphasized by the white lines).

Depending on the bias and the tip quality, terraces are imaged differently. As shown in Fig. 6(a), at positive bias, terraces can be described by lines of different contrasts with various motifs.

At negative bias [Fig. 6(b)] the terraces consist of alternating ordered lines with head-to-tail Y motifs (HTY) and disordered lines where HTY motifs are missing. The STM resolution and the fine structure shown in Fig. 6(b) are routinely obtained.

In both cases, the contrast variation and the FFT of the corresponding STM images are consistent with the (2×1) reconstruction observed by LEED. The lattice parameters measured are $b_s = 28.9 \pm 1.1$ Å in the [010] direction and $c_s = 14.5 \pm 0.6$ Å in the [001] direction, in agreement with the parameter deduced from the LEED analysis. On both sides of the HTY motifs, there are charge-density signatures that are not well resolved.

The bias dependency of the STM contrast should be a consequence of the DOS which is dominated by the Au 5d states below the Fermi level but becomes comparable between Ho 5d and Au 5d states above the Fermi level. Therefore, Au sites are preferentially observed at negative bias while Ho and Au sites are observed at positive bias. It is important to specify here that these two elements are in the same plane (flat) and that the geometric effects are probably smaller than the electronic effects. A similar effect has been reported in the case of the Ag-In-Yb quasicrystalline surface [16,18,37–39].

The atomically resolved STM image in Fig. 6(c) obtained after a change in the tip state gives more information about the origin of the ordered and disordered lines, and the charge density which was not resolved as in Fig. 6(b). These atomically resolved STM images reveal a large variety of different local atomic arrangements along the disordered lines. Among these arrangements, complete (4 bright dots) and incomplete (2 bright dots) rectangles [encircled in black on Fig. 6(c)] tilted away from the [001] direction have been identified. In comparison, the ordered lines form a continuous profile with alternating bright and dim contrasts. Between ordered and disordered lines in inset of Fig. 6(c), there are motifs forming a centered rectangle of 4.45 ± 0.2 Å and 10.1 ± 0.2 Å dimensions.

The (2×1) surface reconstruction observed here is a pure surface effect and not related to specific bulk chemical decoration. Such superstructures do not exist in the bulk as demonstrated by HAADF-STEM and PXRD analyses [33]. Surface reconstruction in Tsai-type approximant has also been reported on the Au-Al-Tb(111) surface where it was found that, depending on the bias, terraces appear with a bright row structure having twofold symmetry (negative bias) or with dimers forming hexagons (at positive bias). These two
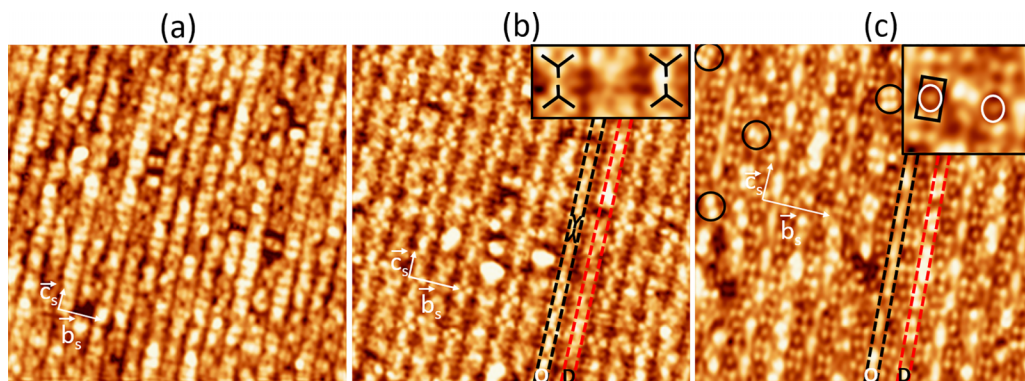

FIG. 6. High-resolution STM image (25×25 nm^2) recorded at $V_b = 1$ V, $I_t = 0.1$ nA (a) and at $V_b = -1.60$ V, $I_t = 0.2$ nA (b) showing the (2×1) surface reconstruction observed in the LEED pattern [inset: zoom on (b)]. (c) Atomic resolution STM image (20×20 nm^2, $V_b = -1.85$ V, $I_t = 0.1$ nA) [inset: zoom on (c)] obtained after a change in the tip state. The region delimited by the black and red dotted lines on (b) and (c) are the ordered and disordered lines, respectively.
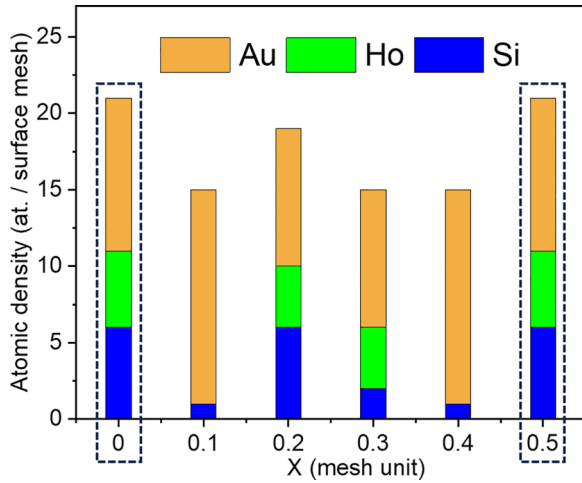
FIG. 7. Atomic density and chemistry as a function of X along the [100] direction. For the plot, the unit cell has been cut into slices ($\Delta X = 0.1$ Å) perpendicular to the [100] direction and the number of atoms of each species was counted for each slice. The dashed rectangles indicate the most Ho-rich planes which are planes intercepting the cluster center which are also the densest.

structures indicate the presence of surface reconstruction which has been related to the desorption of Au/Al atoms from the surface [40,41].

5. Simulated STM images

From the structural investigation of all three high-symmetry surfaces of the icosahedral Ag–In–Yb quasicrystal [16–18], it has been shown that stable planes appearing at the surface are Yb-rich planes and correspond to the bulk planes intersecting the center of the Tsai-type clusters. The stability of the surface planes depends on the atomic density, the chemical composition, and the strength of the chemical bonds involved in the creation of the surface. In the case of Ag-In-Yb QC, the selected surface planes are characterized by a high atomic density and a high Yb content. This rule of selection is valid for the Au-Al-Tb(111) Tsai-type approximant surface where it was found that step heights are three times larger than the separation between two consecutive planes intersecting the cluster centers. This plane selection rule leads to a minimization of the number of dissected bulk icosahedra exposed as topmost surface terminations in the Au-Al-Tb(111) surface [40,41]. In Au-Si-Ho, the step-height value derived from STM data are compatible with the distance separating consecutive planes intercepting the cluster centers. These are dense planes with a high Au and Ho elemental content. By analogy with the Ag-In-Yb case, these planes could be the one selected as surface termination (planes highlighted by dashed rectangles in Fig. 7). Figure 7 shows the atomic density and chemistry of all possible planes perpendicular to the [100] direction. Such surface-plane selection mechanism does not account for the observed (2×1) reconstruction, which is unique with respect to all previous reports on Tsai-type QC approximants.

Following this hypothesis, simulations of STM images were performed for these highest atomic-density planes intercepting the clusters in their equatorial planes. The structural model used for the calculations contains no disorder as
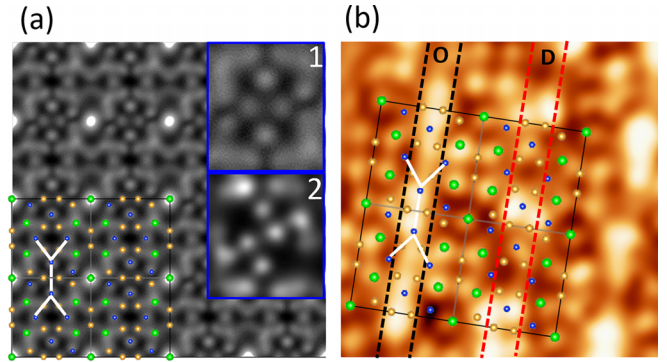

FIG. 8. (a) Simulated STM image calculated from the structure for bias value of -1V [inset 1: zoom on (a), inset 2 corresponds to the relaxed structure of inset 1 for the same bias value]. (b) The surface structural model used in the calculations in (a)–(b) has been superimposed on the atomically resolved STM image ($V_b = -1.85$ V, $I_t = 0.1$ nA). The region delimited by the black and red dotted lines are the ordered and disordered lines, respectively.

explained in Sec. III and all cluster centers are occupied by a Ho atom (no tetrahedron has been taken into consideration). The full occupation of the cluster center with Ho atoms departs from the bulk model but a chemical variant has to be selected for the DFT calculations. Thus, an agreement between the simulated STM image with the experimental image recorded the reconstructed surface is not expected. At most, the simulated images for the (1×1) surface structure could potentially exhibit similarities with local motifs observed experimentally. Figure 8(a) shows the unrelaxed simulated STM image along with the atomic surface model used for the calculations. When superimposing these cluster equatorial planes on experimental STM images [see Fig. 8(b)], a decent agreement is obtained between the model atomic position and the highest experimental contrasts. For instance, the brightest contrast in Fig. 8(a) is related to the Ho atoms and to Si positions. In Fig. 8(b), a similar agreement is found on the ordered line. However, the cluster center reveals experimentally a variety of contrasts as expected from the mixed decoration (Ho or distorted tetrahedron). At this stage, the image contrast in the disordered lines differs from the unreconstructed line. It is related to a different local density of states which could be explained either by atomic desorptions during the surface preparation and/or by local atomic displacements, both phenomena resulting in a (2×1) reconstruction. Ho atoms at the center of Tsai-type cluster correspond to the atoms encircled in white on the inset of Fig. 6(c). They are located at the center of rectangles (see inset in Fig. 6(c)) propagating along the [001] directions and separating ordered and disordered lines in the [010] directions in the experimental STM images. Interestingly, upon structural relaxation of the equatorial plane, the calculations reveal an important layer rumpling along with drastic motifs distortions. Such effect is evidenced when comparing the motifs in the insets 1 and 2 of Fig. 8(a). Moreover, the Ho atoms decorating the cluster centers have shifted away from the mean plane position, i.e. they do not contribute to the STM contrast anymore. Such important atomic rearrangements in- and out-of-plane between (un)relaxed simulations demonstrate a strong tendency to depart from a pure bulk

truncated surface termination. This is highly consistent with the local atomic displacements or/and desorptions observed experimentally which explain the (2×1) reconstruction. The crystallographic model of the equatorial planes contains local configurations compatible with the experimental images.

If the selected surface terminations intercept the cluster centers in Au-Si-Ho, those planes contain the disorder inherent to the mixed decoration of the cluster centers (i.e. circa 52% Ho and 48% tetrahedron). While a (2×1) instead of a (2×2) surface reconstruction can be explained by the surface termination symmetry, the propagating disorder along every other line along the [001] direction may be related to a strain relief mechanism involving local atomic displacements or/and atomic desorption. A similar randomised disorder in the local atomic decoration has already been encountered in a previous work on Al-based approximant where a surface reconstruction was also observed [42]. It would be interesting to explore other index surfaces such as (111) and (110) of Au-Si-Ho, to verify plane selections and to check for surface reconstruction on denser surfaces in order to compare it with the reconstructed Au-Si-Ho(100) surface.

V. CONCLUSION

The surface characterization of Au-Si-Ho(100) demonstrates a bulk truncation at specific planes. These surface terminations correspond to the planes identified as those planes intercepting the Tsai-type clusters in their equatorial planes, consistent with previous reports on Ag-In-Yb Tsai-type quasicrystalline surface [16–18]. In other words, it implies that the Tsai-type cluster centers, decorated either by distorted tetrahedron or RE atom, should appear at the surface. The surface reconstruction (2×1) is not related to the chemical decoration of the bulk. It is a surface effect. Generally, the selection criterion of the surface planes in Tsai/pseudo-Tsai type QCs or ACs is such that it exposes the planes intercepting the center of clusters containing RE. One could think about the possibility of growing a quasicrystalline system with only pseudo-Tsai clusters. This will expose naturally at the surface, RE atoms distributed on an ordered subset of lattice sites, hence potentially forming a complex magnetic structure.

[1] D. Shechtman, I. Blech, D. Gratias, and J. W. Cahn, Metallic phase with long-lange orientational order and no translational symmetry, Phys. Rev. Lett. **53**, 1951 (1984).

[2] P. A. Thiel, Quasicrystal surfaces, Annu. Rev. Phys. Chem. **59**, 129 (2008).

[3] A. Tsai and M. Yoshimura, Highly active quasicrystalline Al-Cu-Fe catalyst for steam reforming of methanol, Appl. Catal. A: Gen. **214**, 237 (2001).

[4] V. Fournée, J. Ledieu, M. Shimoda, M. Krajčí, H.-R. Sharma, and R. McGrath, Thin film growth on quasicrystalline surfaces, Isr. J. Chem. **51**, 1314 (2011).

[5] H. R. Sharma, M. Shimoda, and A. P. Tsai, Quasicrystal surfaces: structure and growth of atomic overlayers, J. Adv. Phys. **56**, 403 (2007).

[6] A. Yamamoto, H. Takakura, and A. Tsai, Structure refinement of i-Al–Pd–Mn quasicrystals by IP-Weissenberg camera data, J. Alloys Compd. **342**, 159 (2002).

[7] D. Gratias, F. Puyraimond, M. Quiquandon, and A. Katz, Atomic clusters in icosahedral F-type quasicrystals, Phys. Rev. B **63**, 024202 (2000).

[8] H. R. Sharma, V. Fournée, M. Shimoda, A. R. Ross, T. A. Lograsso, A. P. Tsai, and A. Yamamoto, Structure of the fivefold surface of the icosahedral Al-Cu-Fe quasicrystal: Experimental evidence of bulk truncations at larger interlayer spacings, Phys. Rev. Lett. **93**, 165502 (2004).

[9] M. Shimoda, H. Sharma, and A.-P. Tsai, Scanning tunneling microscopy study of the fivefold surface of icosahedral Al–Cu–Ru quasicrystal, Surf. Sci. **598**, 88 (2005).

[10] B. Unal, T. A. Lograsso, A. Ross, C. J. Jenks, and P. A. Thiel, Terrace selection during equilibration at an icosahedral quasicrystal surface, Phys. Rev. B **71**, 165411 (2005).

[11] J. Ledieu, R. McGrath, R. D. Diehl, T. A. Lograsso, D. W. Delaney, Z. Papadopolos, and G. Kasner, Tiling of the fivefold surface of $Al_{70}Pd_{21}Mn_9$, Surf. Sci. **492**, L729 (2001).

[12] Z. Papadopolos, G. Kasner, J. Ledieu, E. J. Cox, N. V. Richardson, Q. Chen, R. D. Diehl, T. A. Lograsso, A. R. Ross, and R. McGrath, Bulk termination of the quasicrystalline fivefold surface of $Al_{70}Pd_{21}Mn_9$, Phys. Rev. B **66**, 184207 (2002).

[13] H. Takakura, C. P. Gómez, A. Yamamoto, M. De Boissieu, and A. P. Tsai, Atomic structure of the binary icosahedral Yb–Cd quasicrystal, Nat. Mater. **6**, 58 (2007).

[14] A. P. Tsai, J. Q. Guo, E. Abe, H. Takakura, and T. J. Sato, A stable binary quasicrystal, Nature (London) **408**, 537 (2000).

[15] A.-P. Tsai, A. Inoue, and T. Masumoto, Preparation of a new Al-Cu-Fe quasicrystal with large grain sizes by rapid solidification, J. Mater. Sci. Lett. **6**, 1403 (1987).

[16] C. Cui, P. J. Nugent, M. Shimoda, J. Ledieu, V. Fournée, A. P. Tsai, R. McGrath, and H. R. Sharma, The atomic structure of the threefold surface of the icosahedral Ag–In–Yb quasicrystal, J. Phys.: Condens. Matter **24**, 445011 (2012).

[17] C. Cui, P. J. Nugent, M. Shimoda, J. Ledieu, V. Fournée, A. P. Tsai, R. McGrath, and H. R. Sharma, Structure of the twofold surface of the icosahedral Ag–In–Yb quasicrystal, J. Phys.: Condens. Matter **26**, 015001 (2014).

[18] H. R. Sharma, M. Shimoda, K. Sagisaka, H. Takakura, J. A. Smerdon, P. J. Nugent, R. McGrath, D. Fujita, S. Ohhashi, and

A. P. Tsai, Structure of the fivefold surface of the Ag-In-Yb icosahedral quasicrystal, Phys. Rev. B **80**, 121401(R) (2009).

[19] G. Gebresenbut, T. Shiino, D. Eklöf, D. C. Joshi, F. Denoel, R. Mathieu, U. Häussermann, and C. Pay Gómez, Atomic-scale tuning of Tsai-type clusters in RE–Au–Si systems (RE = Gd, Tb, Ho), Inorg. Chem. **59**, 9152 (2020).

[20] G. H. Gebresenbut, R. Tamura, D. Eklöf, and C. P. Gómez, Syntheses optimization, structural and thermoelectric properties of 1/1 Tsai-type quasicrystal approximants in RE–Au–SM systems (RE=Yb, Gd and SM=Si, Ge), J. Phys.: Condens. Matter **25**, 135402 (2013).

[21] G. H. Gebresenbut, T. Shiino, M. S. Andersson, N. Qureshi, O. Fabelo, P. Beran, D. Qvarngård, P. Henelius, A. Rydh, R. Mathieu, P. Nordblad, and C. Pay Gomez, Effect of pseudo-Tsai cluster incorporation on the magnetic structures of $R-Au-Si$ (R = Tb, Ho) quasicrystal approximants, Phys. Rev. B **106**, 184413 (2022).

[22] G. H. Gebresenbut, M. S. Andersson, P. Nordblad, M. Sahlberg, and C. Pay Gómez, Tailoring magnetic behavior in the Tb-Au-Si quasicrystal approximant system, Inorg. Chem. **55**, 2001 (2016).

[23] W. Bajoun Mbajoun, Y.-C. Huang, G. H. Gebresenbut, C. P. Gómez, V. Fournée, and J. Ledieu, Surface reactivity of the Au-Si-Ho quasicrystalline 1/1 approximant, Isr. J. Chem., e202300118 (2023).

[24] G. Kresse and J. Hafner, *Ab initio* molecular dynamics for liquid metals, Phys. Rev. B **47**, 558 (1993).

[25] G. Kresse and J. Hafner, *Ab initio* molecular-dynamics simulation of the liquid-metal-amorphous-semiconductor transition in germanium, Phys. Rev. B **49**, 14251 (1994).

[26] G. Kresse and J. Furthmüller, Efficient iterative schemes for *ab initio* total-energy calculations using a plane-wave basis set, Phys. Rev. B **54**, 11169 (1996).

[27] G. Kresse and J. Furthmüller, Efficiency of *ab-initio* total energy calculations for metals and semiconductors using a plane wave basis set, Comput. Mater. Sci. **6**, 15 (1996).

[28] P. E. Blochl, Projector augmented-wave method, Phys. Rev. B **50**, 17953 (1994).

[29] G. Kresse and D. Joubert, From ultrasoft pseudopotentials to the projector augmented-wave method, Phys. Rev. B **59**, 1758 (1999).

[30] J. P. Perdew, K. Burke, and M. Ernzerhof, Generalized gradient approximation made simple, Phys. Rev. Lett. **77**, 3865 (1996).

[31] J. P. Perdew, K. Burke, and M. Ernzerhof, Erratum: Generalized gradient approximation made simple, Phys. Rev. Lett. **78**, 1396(E) (1997).

[32] K. Okhotnikov, T. Charpentier, and S. Cadars, Supercell program: a combinatorial structure-generation approach for the local-level modeling of atomic substitutions and partial occupancies in crystals, J. Cheminf. **8**, 17 (2016).

[33] W. Bajoun Mbajoun, V. Sršan, Y.-C. Huang, G. H. Gebresenbut, C. Pay Gómez, S. Migot-Choux, J. Ghanbaja, S. Šturm, V. Fournée, and J. Ledieu, STEM structural investigation of RE-Au-Si 1/1 approximants, Isr. J. Chem., e202300117 (2023).

[34] D. Biswas, N. Sahadev, G. Adhikary, G. Balakrishnan, and K. Maiti, Evolution of the electronic structure of HoB_4 with temperature, Phys. Rev. B **88**, 134405 (2013).

[35] T. Shishido, M. Oku, T. Sasaki, H. Iwasaki, H. Kishi, H. Horiuchi, and T. Fukuda, XPS and magnetic measurements for perovskite-type $HoRh_3B$, J. Alloys Compd. **283**, 91 (1999).

[36] C. W. Chuang, F. M. F. de Groot, Y. F. Liao, Y. Y. Chin, K. D. Tsuei, R. Nirmala, D. Malterre, and A. Chainani, Hard x-ray photoemission spectroscopy of GdNi and HoNi, Phys. Rev. B **102**, 165127 (2020).

[37] H. R. Sharma, G. Simutis, V. R. Dhanak, P. J. Nugent, C. Cui, M. Shimoda, R. McGrath, A. P. Tsai, and Y. Ishii, Valence band structure of the icosahedral Ag-In-Yb quasicrystal, Phys. Rev. B **81**, 104205 (2010).

[38] D. Burnie, S. Coates, R. McGrath, and H. R. Sharma, Bias-voltage dependent STM images from the 2–fold surface of the icosahedral Ag-In-Yb quasicrystal, J. Phys. Conf. **1458**, 012017 (2020).

[39] Y. Ishii and T. Fujiwara, Hybridization mechanism for cohesion of Cd-based quasicrystals, Phys. Rev. Lett. **87**, 206408 (2001).

[40] S. Coates, D. Burnie, H. R. Sharma, and R. McGrath, Scanning tunnelling microscopy studies of Tsai-type quasicrystal approximants, Isr. J. Chem., e202300116 (2023).

[41] S. Coates, K. Nozawa, M. Fukami, K. Inagaki, M. Shimoda, R. McGrath, H. R. Sharma, and R. Tamura, Atomic structure of the (111) surface of the antiferromagnetic 1/1 Au-Al-Tb approximant, Phys. Rev. B **102**, 235419 (2020).

[42] J. Ledieu, E. Gaudry, K. Pussi, T. Jarrin, P. Scheid, P. Gille, and V. Fournée, Reconstruction of the $Al_{13}Ru_4$(010) approximant surface leading to anisotropic molecular adsorption, J. Phys. Chem. C **121**, 22067 (2017).